JACS
JOURNAL OF THE AMERICAN CHEMICAL SOCIETY
pubs.acs.org/JACS
Article

A Covalent Organic Framework for Cooperative Water Oxidation

Suvendu Karak, Vladimir Stepanenko, Matthew A. Addicoat, Philipp Keßler, Simon Moser, Florian Beuerle,* and Frank Würthner*

Cite This: J. Am. Chem. Soc. 2022, 144, 17661−17670
Read Online
ACCESS | Metrics & More | Article Recommendations | Supporting Information

ABSTRACT: The future of water-derived hydrogen as the "sustainable energy source" straightaway bets on the success of the sluggish oxygen-generating half-reaction. The endeavor to emulate the natural photosystem II for efficient water oxidation has been extended across the spectrum of organic and inorganic combinations. However, the achievement has so far been restricted to homogeneous catalysts rather than their pristine heterogeneous forms. The poor structural understanding and control over the mechanistic pathway often impede the overall development. Herein, we have synthesized a highly crystalline covalent organic framework (COF) for chemical and photochemical water oxidation. The interpenetrated structure assures the catalyst stability, as the catalyst's performance remains unaltered after several cycles. This COF exhibits the highest ever accomplished catalytic activity for such an organometallic crystalline solid-state material where the rate of oxygen evolution is as high as ~26,000 μmol L^{-1} s^{-1} (second-order rate constant $k \approx 1650$ μmol L s^{-1} g^{-2}). The catalyst also proves its exceptional activity ($k \approx 1600$ μmol L s^{-1} g^{-2}) during light-driven water oxidation under very dilute conditions. The cooperative interaction between metal centers in the crystalline network offers 20−30-fold superior activity during chemical as well as photocatalytic water oxidation as compared to its amorphous polymeric counterpart.

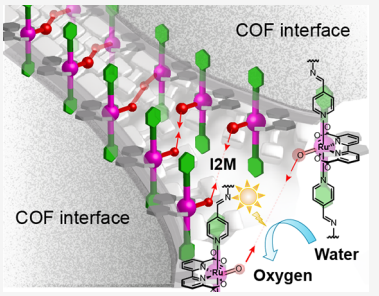

INTRODUCTION

The pursuit of sustainable energy sources that eliminate concerns over depleting fossil fuel resources and their environmental impact is imminent.[1] Harnessing solar energy *via* water splitting, inspired by the oxygen-evolving complex in natural photosystem II (OEC-PSII), could facilitate the alleviation of this crisis.[2] However, the prime impediment of this sustainable cycle remains the anodic half-reaction, consisting of the four-electron oxidation process of water into molecular oxygen ($2H_2O \rightarrow O_2 + 4e^- + 4H^+$).[3] The quest for long-term solutions has led to the advancement of transition metal-based homogeneous water oxidation catalysts (WOCs).[4,5] In this regard, molecular Ru catalysts have emerged as forerunners by successfully achieving low overpotentials and high turnover frequency, comparable to the natural Mn_4CaO_5 cluster.[6,7]

Although homogeneous catalysts typically offer superior performance, practical considerations urge for the implementation of heterogeneous catalysts to facilitate processable and durable devices. Hence, there is a dire necessity for the transformation of highly active molecular catalysts into heterogeneous systems without significant loss of performance. In this regard, anchoring individual catalysts at solid substrates via covalent or noncovalent interactions seems straightforward.[8−11] However, such integrated catalytic systems usually comprise of low active surface areas, poor accessibility of the catalytic centers, or gradual detachment from the interface. In many cases, the immobilization of the molecular catalyst impedes detailed mechanistic understanding or induces different reaction pathways. For instance, the mechanism for the O−O bond formation might switch from the interaction of two metal−oxyl radicals (I2M) to water nucleophilic attack (WNA) after catalyst immobilization.[12,13] Thus, for any further improvement of the catalytic performance in heterogeneous water splitting, a better understanding is necessary for the crucial mechanistic details and the factors that govern these pathways.[14] In this regard, the modular construction of well-ordered molecular frameworks from small-molecule toolkits may combine (i) the structural precision of molecular homogeneous catalysts with key advantages for heterogeneous catalysis such as (ii) the recyclability and durability of polymeric frameworks, (iii) densely packed structures that are less prone to air oxidation, and (iv) the emergence of cooperative interactions between multiple active centers on the interfaces.

In this regard, two-dimensional (2D) covalent organic framework (COF) materials have recently made their mark on the photocatalytic hydrogen evolution reaction (HER).[15−20] So far, however, limited progress has been made regarding the photocatalytic oxygen evolution reaction (OER) owing to its complicated multicomponent nature and energetically uphill

Received: July 11, 2022
Published: September 15, 2022

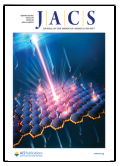

https://doi.org/10.1021/jacs.2c07282
J. Am. Chem. Soc. 2022, 144, 17661−17670

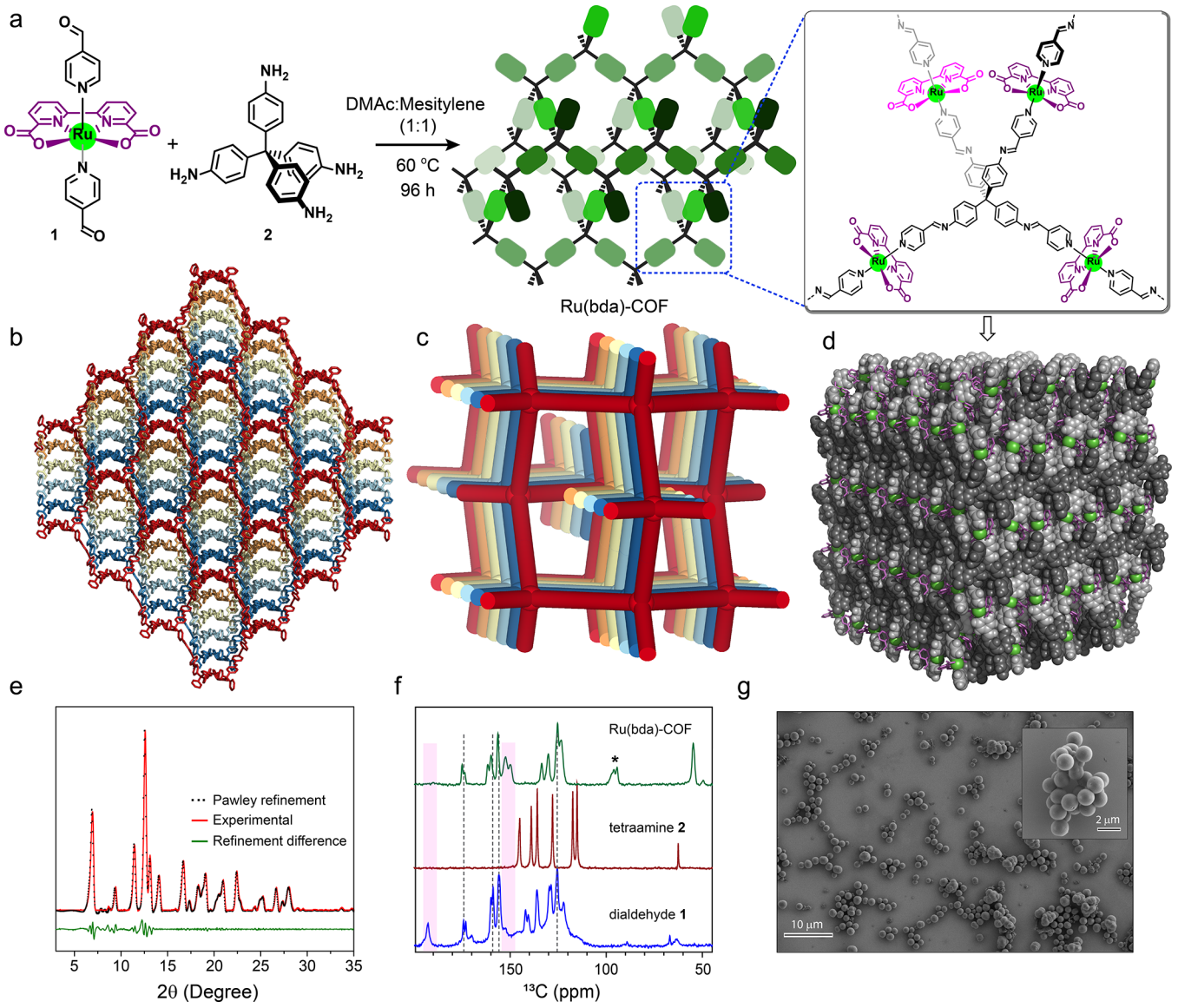

Figure 1. Synthesis and characterization of Ru(bda)-COF. (a) Synthesis of microcrystalline Ru(bda)-COF from dialdehyde **1** and tetraamine **2**. (b) Densely packed interpenetrated network of COF. (c) Cartoon representation of dia-c5 net adopted by COF with 5-fold interpenetration. The net has been created by connecting the centers of the tetrahedral unit. (d) Long-range ordering of the Ru centers (green) on the interface of the interpenetrated dia-c5 net. Ru sites are arranged sequentially in a long-range order. (e) Pawley refinement of the dia-c5 COF. (f) CP-MAS ^{13}C NMR spectra of Ru(bda)-COF (green), tetraamine **2** (red), and dialdehyde **1** (blue). (g) Scanning electron microscopy (SEM) image of Ru(bda)-COF.

anodic half-reaction.[21−26] The common use of rather ill-defined Pt-based (for HER) and Ru-based (for OER) cocatalysts during water splitting deters the complete perception of the active catalytic sites and intricacies of the reaction cycles.[27,28] In addition, the usage of organic solvents adds further concerns on the sustainability of these heterogeneous catalysts.

But significant improvement might be achieved with pristine COFs,[29,30] considering that the precise positioning of active WOCs could offer abundant accessible sites within the COF backbone.[31,32] The interpenetrated (three-dimensional) 3D network might also boost the much-needed catalytic stability and recyclability of heterogeneous systems in combination with the desired advantages of a molecular catalyst.

Here, we report on the modular implementation of Ru(bda)-based (bda = 2,2′-bipyridine-6,6′-dicarboxylate) dialdehyde **1** as an integral component into both crystalline and amorphous 3D imine polymers. The reversible imine bonding endeavors the building blocks' connectivity and renders a framework through covalent bonding. Whereas the amorphous Ru(bda)-polymer showed modest catalytic activity in both chemical and photochemical water oxidation, crystalline Ru(bda)-COF revealed an up to 30 times superior performance compared to the similarly cross-linked amorphous polymer. The COF showcases very good catalytic activity where the rate of oxygen evolution is as high as ∼26,000 μmol L^{-1} s^{-1}. Several consecutive catalytic cycles in both acidic and neutral media indicate the durability and recyclability of Ru(bda)-COF. Extensive mechanistic studies including H/D kinetic isotope effect (KIE) studies and comparison to molecular model systems provided key insights into the O−O bond formation pathway (I2M versus WNA) for such

https://doi.org/10.1021/jacs.2c07282
J. Am. Chem. Soc. 2022, 144, 17661−17670

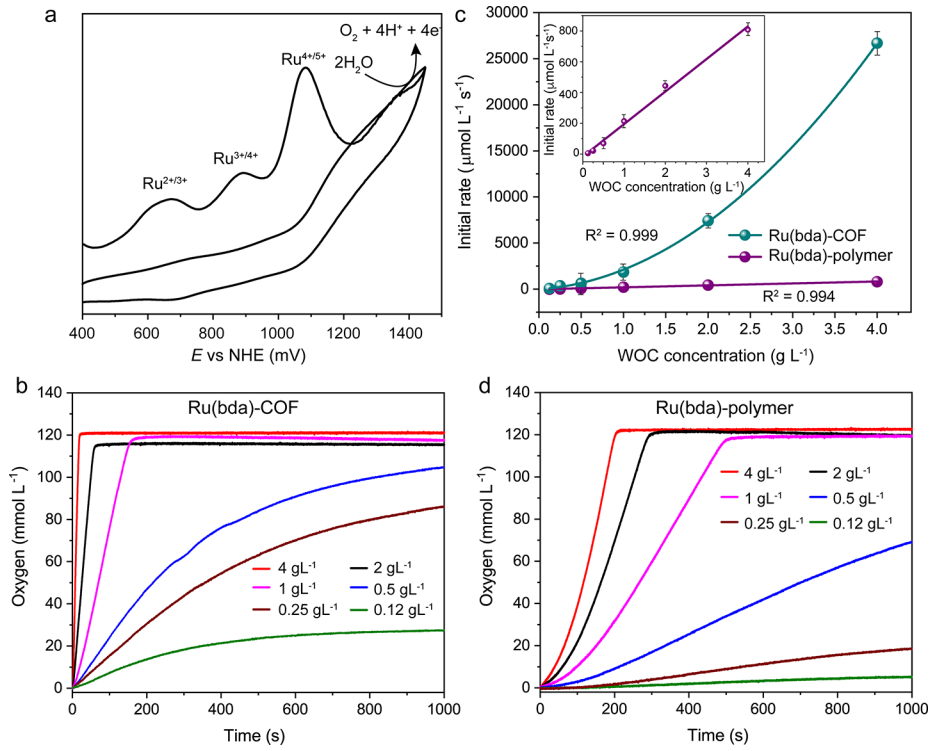

Figure 2. Redox properties and chemical water oxidation catalysis for WOCs. (a) Cyclic and differential pulse voltammograms of Ru(bda)-COF deposited on a multiwalled carbon nanotube-coated glassy carbon disk electrode. Time-dependent O_2 evolution for various amounts of (b) Ru(bda)-COF and (d) Ru(bda)-polymer (3.4 mL of aqueous solution using CAN (0.54 M) as a sacrificial oxidant, 20 °C, pH = 1 (CF_3SO_3H:H_2O), 1000 rpm stirring speed). (c) Plots of initial catalysis rates (obtained by linear fit of O_2 evolution curve for the first 2 or 150 s of catalysis for the COF and polymer, respectively) versus WOC concentration with corresponding linear (Ru(bda)-polymer, purple) and quadratic (Ru(bda)-COF, cyan) regression fit.

heterogeneous catalysts. Apparently, the nanoscale recurring arrangement of the active centers within Ru(bda)-COF allows for a concurrent O−O bond formation in a cooperative fashion.

RESULTS AND DISCUSSION

Synthesis and Characterization. The high activity of the Ru(bda) unit[6,7] as WOC has prompted us to implement such molecular catalysts as integral components into highly ordered framework materials. As a versatile building block for imine COFs, we synthesized linear linker Ru(bda) dialdehyde **1** (see the Supporting Information for details) by adopting a well-established synthetic protocol. The equatorial bda ligand possesses a wide O−Ru−O angle of 123.7°, unlike the 90° angle of an ideal octahedral geometry (Figure S6). The large bite angle allows coordination expansion *via* binding of H_2O that could further facilitate the Ru center to reach a high-valent oxo state, which is a key step toward water oxidation.[6,7] The two carboxylate groups also stabilize high-oxidation states at the metal. Thus, for the successful integration of the Ru(bda) system in a 3D ordered framework, we have investigated the imine condensation between dialdehyde **1** and tetra-(4-anilyl)methane **2** (1:2 molar ratio) in various solvents (Table S1). For most polar solvents such as DMSO, THF, MeOH, or DMF, no precipitate but formation of soluble oligomers and small molecular fragments was observed. Only after reaction in highly polar *N*,*N*-dimethylacetamide (DMAc) at 120 °C for 24 h, amorphous imine framework Ru(bda)-polymer could be isolated in 75% yield. Upon further optimization, microcrystalline Ru(bda)-COF was obtained in 55% yield after imine condensation in a 1:1 mixture of polar DMAc and nonpolar mesitylene at 60 °C for 4 days (Figure 1a and Figures S5 and S7−S10). Both precipitates were washed with DMAc and anhydrous THF or dioxane followed by drying under high vacuum.

The formation of extended imine polymers was proven by Fourier transform infrared (FTIR) spectroscopy. The occurrence of C═C and C═N stretching modes at 1548−1555 cm^{-1} and 1620 cm^{-1}, respectively, and the disappearance of the N−H vibrations of the amino groups in **2** confirm the formation of a cross-linked imine backbone for both Ru(bda)-COF and Ru(bda)-polymer (Figure S18). For the crystalline COF, the chemical connectivity of the framework was further corroborated by solid-state CP-MAS ^{13}C NMR spectroscopy (Figure 1f). The lack of any aldehyde signal around 190 ppm confirms the complete conversion and the absence of any free dialdehyde **1** within the COF-matrix. The chemical shift of 152 ppm for the newly emerged imine moieties is in good agreement with a literature report.[33] For amorphous Ru(bda)-polymer, only very broad and non-assignable spectra were obtained. The thermogravimetric analysis (TGA) of Ru(bda)-COF and Ru(bda)-polymer under a N_2 atmosphere revealed a slightly higher thermal stability up to 250 °C for the crystalline COF compared to the amorphous polymer (Figure S19).

The nanoscale structure and ordering of the materials were investigated by powder X-ray diffraction (PXRD). The lack of any defined reflections for Ru(bda)-polymer confirms the amorphous structure of this material (Figure S8). For as-synthesized Ru(bda)-COF however, the experimental PXRD pattern clearly reveals the presence of crystalline domains

https://doi.org/10.1021/jacs.2c07282
J. Am. Chem. Soc. 2022, 144, 17661−17670

differing from the starting materials (Figure 1e and Figure S7). 3D COFs with dia topology typically crystallize in highly symmetrical tetragonal space groups.[34] To account for the steric demand and potential disorder of the out-of-plane bda ligands however, we considered a lower symmetry for this peculiar framework. After Pawley refinement with rigid body restraints, a refined unit cell (P_1, a = 18.3 Å, b = 19.0 Å, c = 20.1 Å, α = 92.4°, β = 89.6°, γ = 87.3°, R_{wp} = 7.35%, and R_p = 8.35%) was obtained and the first and most intense reflections at 2θ = 6.8, 9.4, 11.4, 12.5, and 13.1 were indexed to the ⟨101⟩, ⟨200⟩, ⟨211⟩, ⟨202⟩, and ⟨220⟩ planes, respectively. To provide a structural model for Ru(bda)-COF, we constructed several periodical dia-nets from precursors **1** and **2** with varying dimensions of the unit cell or degree of interpenetration (4- to 7-fold) and simulated PXRD patterns for these structures (see the Supporting Information for more details). From these data, the best match with the experimental PXRD pattern was obtained for the dia-c5 structure with 5-fold interpenetration that is shown in Figure 1b−d and Figures S13−S15. The remaining discrepancies at wider angles are presumably caused by disorder and rotations of the equatorial bda ligands (Figures S16 and S17), which cannot be accurately included in these simplified static models. As shown for the models in Figure 1b,d, Ru(bda)-COF crystallizes in a rather dense packing and the measured surface areas of 30 and 139 $m^2\ g^{-1}$ (Ar adsorption at 87.3 K, Figure S20) for Ru(bda)-COF and Ru(bda)-polymer, respectively, indicate that both materials are nonporous with the obtained areas rather correlating with the outer surface of the nanoparticles. Interestingly, the higher value for the amorphous polymer suggests a significantly lower surface roughness for Ru(bda)-COF compared to Ru(bda)-polymer. The morphology of both samples was further analyzed by scanning electron microscopy (SEM). Generally, the as-synthesized Ru(bda)-COF showed a sheet-like morphology in the range of 5−15 μm (Figures S21a−d and S22a). However, a close inspection revealed that individual sheets consist of spherical COF nanoparticles (Figure S14c,e−h). Ultrasound sonication of a COF suspension in water for 30 min resulted in the complete disruption of the sheets into spherical nanoparticles in the range of 70−2000 nm (Figure 1g and Figures S21l, S22b, S40d, and S42d). Through polymeric membrane filtration, different size fractions of Ru(bda)-COF were obtained (Figure S23).

The redox properties of both Ru(bda)-COF and Ru(bda)-polymer were investigated by cyclic and differential pulse voltammetry. Electrochemical studies at pH = 7 (phosphate buffer) highlight all three redox states of the catalyst in aqueous solution. Three oxidation peaks versus a normal hydrogen electrode (NHE) at +0.67, +0.89, and +1.08 V and +0.69, +0.93, and +1.12 V were measured for Ru(bda)-COF and Ru(bda)-polymer, respectively, which refer to the formal redox pairs $Ru^{2+/3+}$, $Ru^{3+/4+}$, and $Ru^{4+/5+}$ within the polymeric matrices (Figure 2a). These potentials (Figure S25 and Table S3) are, in particular for the crystalline COF, slightly lower than those from a previous literature report for molecular Ru(bda) catalysts.[9] This lowering in oxidation potential might be attributed to the ordered nanostructure of the extended Ru(bda) domains, in which COOH units from bda linkers of neighboring threads participate in weak hydrogen bonding (Figure S26). As water oxidation catalysis typically involves highly oxidized Ru^{5+} species, the lower potentials in the ordered frameworks might facilitate the O_2 evolution reaction. Altogether, the combined analytical data provide convincing evidence for the dense and highly ordered alignment of molecularly defined Ru(bda) moieties at the interface of spherical Ru(bda)-COF nanoparticles. As a reference material, Ru(bda)-polymer has the same connectivity of the molecular building units but lacks the nanoscale order of the catalytically active centers.

Chemical Water Oxidation. O_2 evolution for aqueous suspensions (pH = 1) of Ru(bda)-COF and Ru(bda)-polymer in the presence of cerium(IV) ammonium nitrate (CAN) as a sacrificial electron acceptor (SEA) was measured with a pressure transducer. To screen for optimum reaction conditions, initial rates of O_2 formation were obtained for the first 2 s of catalysis at a fixed catalyst loading (1.0 $g\ L^{-1}$ Ru(bda)-COF) and varying amounts of CAN (Figure S27 and Table S4).

The observation of significantly lower rates at higher CAN concentration indicates that the catalysis occurs on the surface of the COF particles. With increasing concentration, CAN molecules start to block the catalytically active sites at the interface, which restricts the availability of water molecules around the Ru centers, thus resulting in reduced performance. For further measurements, we chose 0.54 M as the excess concentration for CAN to achieve reasonable values for both reaction rates and turnover. For amorphous Ru(bda)-polymer, modest initial rates up to 809 $\mu mol\ L^{-1}\ s^{-1}$ at 4.0 $g\ L^{-1}$ and first-order kinetics ($k_{Ru(bda)\text{-polymer}}$ = 211 $\mu mol\ g^{-1}\ s^{-1}$) were obtained (Figure 2c,d and Figure S28). The sigmoidal shape of the O_2 evolution curves for all concentrations (Figure 2d) indicates a significant induction period and slow activation of the solid material, which is presumably caused by the limited accessibility of the active catalysts being randomly distributed on the rough surface and buried in the thread-like morphology. For crystalline Ru(bda)-COF however, a much higher and instantaneous catalytic activity with initial rates as high as 26,600 $\mu mol\ L^{-1}\ s^{-1}$ at 4.0 $g\ L^{-1}$ was observed (Figure 2b and Table S5). This up to 30-fold increase in activity for the crystalline framework compared to the amorphous framework impressively illustrates the beneficial effect of long-range order on catalytic performance. Surprisingly, a plot of initial catalysis rate *versus* Ru(bda)-COF concentration reveals second-order kinetics ($k_{Ru(bda)\text{-COF}}$ = 1660 $\mu mol\ L\ g^{-2}\ s^{-1}$), which seems unusual for a heterogeneous catalyst (Figure 2c). The different kinetics are indicative of a change in O−O bond formation mechanism (see detailed discussion below). Encouragingly, both the catalytic performance and the chemical and structural integrity of Ru(bda)-COF were fully retained even after several consecutive cycles (Figures S29−S31). Crystallite size calculation from PXRD data using the Williamson−Hall (W−H) plot method confirmed that there is no significant change in the structure and domain sizes before (17 nm) and after (14 nm) five catalytic cycles (Figures S32 and S33). Apparently, the highly interpenetrated 3D structure of crystalline Ru(bda)-COF provides the much-needed framework stability[31,35] while still maintaining molecular control on the chemical environment for the catalytic units. The highest TON for heterogeneous water oxidation is also around five times higher for the COF as compared to the polymer (Table S6). As another control experiment to probe the stability of the COF backbone, we tested the filtrate of a Ru(bda)-COF suspension for water oxidation (Figure S34). No indication for O_2 evolution during the whole measurement eliminates the possibility of any degradation of the Ru(bda) unit into the

https://doi.org/10.1021/jacs.2c07282
J. Am. Chem. Soc. 2022, 144, 17661−17670

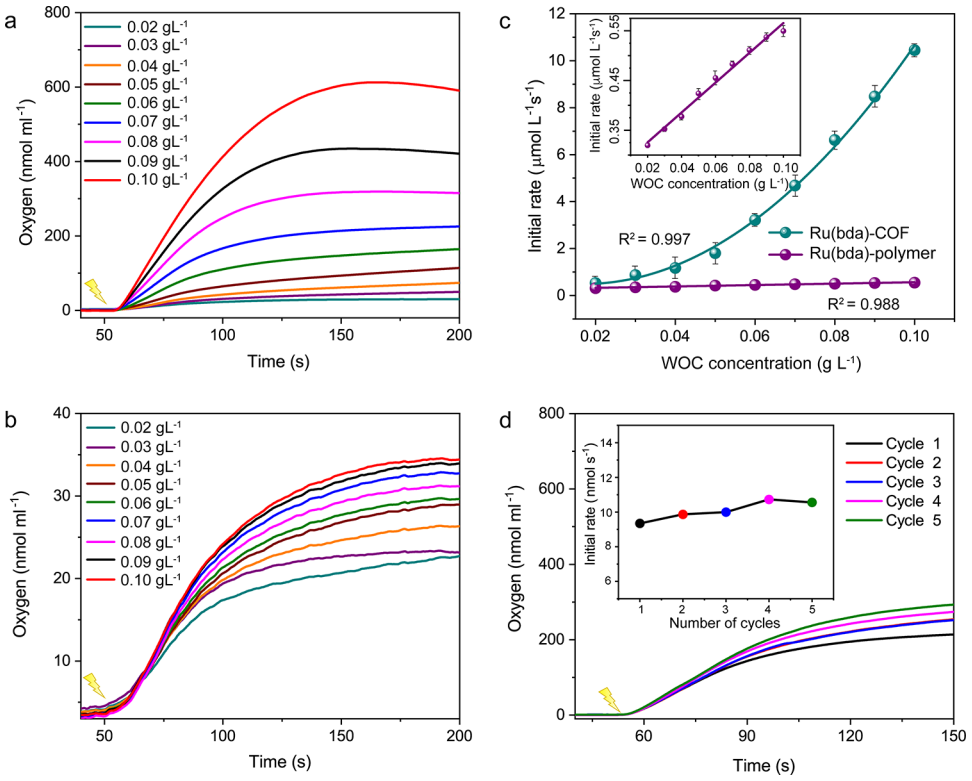

Figure 3. Photochemical water oxidation catalysis for Ru(bda)-based WOCs. Time-dependent O_2 evolution for various amounts of (a) Ru(bda)-COF and (b) Ru(bda)-polymer (2 mL solution of 3:7 MeCN/aqueous phosphate buffer (pH = 7), $c([Ru(bpy)_3]Cl_2)$ = 1.66 mM, $c(Na_2S_2O_8)$ = 41 mM; irradiation started at t = 50 s and O_2 formation was measured with a Clark-type electrode setup). (c) Plots of initial catalysis rates (obtained by linear fit of O_2 evolution curve between 65 and 75 s) versus WOC concentration with corresponding linear (Ru(bda)-polymer, purple) and quadratic (Ru(bda)-COF, cyan) regression fit. (d) Recyclability test to five consecutive cycles for Ru(bda)-COF (2 mL solution of 3:7 MeCN/aqueous phosphate buffer (pH = 7), c(Ru(bda)-COF) = 0.07 g L^{-1}, $c([Ru(bpy)_3]Cl_2)$ = 1.66 mM, $c(Na_2S_2O_8)$ = 41 mM; irradiation started at t = 50 s and O_2 formation was measured with a Clark-type electrode setup).

solution phase during chemical water oxidation with the heterogeneous catalyst. Additionally, we performed energy-dispersive X-ray (EDX) analysis for a filtrated solution after catalysis. The absence of any Ru signals rules out the leakage of any soluble catalytically active species during the chemical water oxidation (Figure S35).

Photocatalytic Water Oxidation. The accomplishment of chemical water oxidation further motivated us to establish a more complex three-component photocatalytic water oxidation system for heterogeneous Ru(bda) polymers. For this purpose, $[Ru(bpy)_3]Cl_2$ and sodium persulfate ($Na_2S_2O_8$) were used as the photosensitizer (PS) and SEA, respectively. The SEA initially oxidizes the photogenerated PS* to PS$^+$, which then oxidizes the WOC repeatedly to achieve the pivotal Ru^{5+} state (Figure S36).

Extensive screening of reaction conditions for this multi-component system revealed the highest O_2 evolution at a particular WOC concentration (measured with a Clark-type electrode) for c_{PS} = 1.66 mM and c_{SE} = 41 mM in a 3:7 mixture of MeCN and an aqueous phosphate buffer solution at pH = 7 (Figures S37 and S38). Like in chemical water oxidation, crystalline Ru(bda)-COF nanoparticles showed a significantly higher catalytic activity compared to amorphous Ru(bda)-polymer (Figure 3a,b). Even at a very low catalyst loading of 0.1 g L^{-1}, an initial rate of 10.4 μmol L^{-1} s^{-1} was achieved for Ru(bda)-COF, which was roughly 20 times higher than for Ru(bda)-polymer (0.5 μmol L^{-1} s^{-1}). To the best of our knowledge, this is by far the highest rate achieved so far for any COF-based heterogeneous water splitting systems for either H_2 or O_2 evolution (see Table S10 for a comparison with literature benchmarks). Again, plots of the initial rates versus WOC concentration revealed second- and first-order kinetics for Ru(bda)-COF and Ru(bda)-polymer, respectively (Figure 3c). By quadratic or linear regression fits, second- and first-order rate constants of 1072 μmol L g^{-2} s^{-1} and 3.0 μmol g^{-1} s^{-1} were obtained for the crystalline and amorphous frameworks, respectively (Figure S39). These data suggest that the O−O bond formation follows a similar mechanism for both chemical and photochemical water oxidation. The different performance and presumed switch in mechanism between crystalline Ru(bda)-COF and amorphous Ru(bda)-polymer impressively demonstrate the importance of order and molecular precision for efficient heterogeneous catalysis. For Ru(bda)-COF, a recyclability test confirmed its reusability and chemical integrity, as the turnover for this multicomponent photocatalytic water oxidation system did not decrease even after five consecutive cycles (Figure 3d). For Ru(bda)-polymer, a drastically reduced amount of O_2 is generated (Figure 3b), as the significantly lower activity of the amorphous catalyst makes the degradation of the PS the limiting factor in this system.

Mechanistic Investigation of Water Oxidation. For molecular Ru WOCs, two main mechanistic pathways are discussed in the literature that differ in the O−O bond formation step: (i) the interaction of two highly oxidized Ru−oxyl radicals (I2M) or (ii) the nucleophilic attack of a water

https://doi.org/10.1021/jacs.2c07282
J. Am. Chem. Soc. 2022, 144, 17661−17670

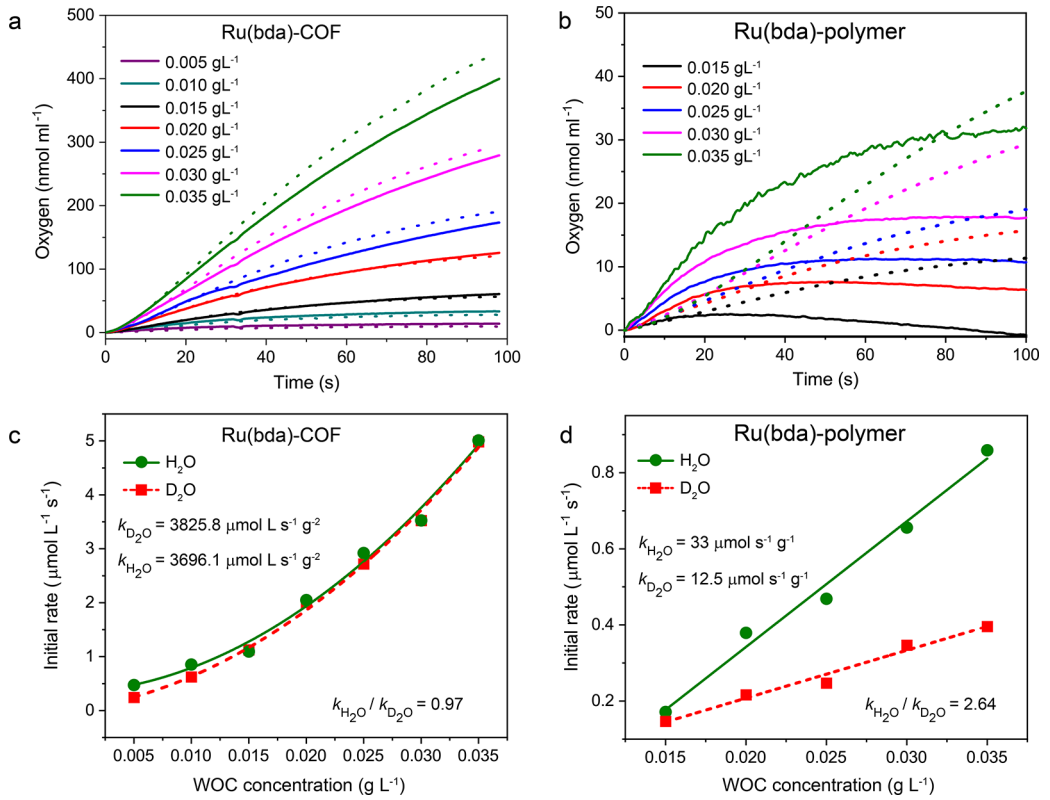

Figure 4. Kinetic isotope effect measurements for Ru(bda)-based WOCs. Time-dependent O_2 evolution during chemical water oxidation for various amounts of (a) Ru(bda)-COF and (b) Ru(bda)-polymer (2 mL of H_2O (solid lines) or D_2O (dashed lines) using CAN (0.53 M) as a sacrificial oxidant, pH = 1, 20 °C, 100 rpm stirring speed; O_2 formation was measured with a Clark-type electrode setup). Plots of initial catalysis rates versus (c) Ru(bda)-COF and (d) Ru(bda)-polymer concentration (second- and first-order rate constants were determined by linear regression fit for plots of initial rates versus square of Ru(bda)-COF concentration or Ru(bda)-polymer, respectively (Figure S46)).

molecule at one highly oxidized Ru-oxyl species (WNA). Usually, both pathways can easily be distinguished for homogeneous catalysts as I2M or WNA WOCs show second- or first-order kinetics, respectively. For immobilized I2M catalysts, disorder and restricted motion typically prevent the required proximity of individual catalysts, thus leading to a switch to the WNA mechanism and significant loss in performance. For Ru(bda)-COF however, chemical and photochemical water oxidation is second order in COF concentration, which indicates that two COF particles are involved in the rate-determining step (RDS). For Ru(bda)-polymer instead, the obtained first-order kinetics point to either an intrapolymer process or a switch to the WNA mechanism. To get more insight into mechanistic details, we have investigated the primary kinetic isotope effect (KIE) for polymeric Ru(bda) WOCs.

In the case of WNA, a proton-coupled process is involved in the RDS, thus leading to a ratio of k_{H_2O}/k_{D_2O} of around 2 when performing the water oxidation in both H_2O and D_2O. For I2M, a KIE of around 0.7−1.5 is expected as no protons are involved in the dimerization of two metal oxides as the RDS. Figure 4 shows the O_2 evolution curves and plots of initial rates versus WOC concentration. For Ru(bda)-polymer, linear fits and a KIE of 2.64 were observed, as expected, thus proving a proton-coupled unimolecular RDS (Figure 4b,d). By contrast, a KIE of 0.97 for the quadratic fits indicated a bimolecular RDS without proton abstraction for Ru(bda)-COF (Figure 4a,c). Based on the combined analytical data, we propose the following mechanisms for heterogeneous Ru(bda) WOCs. For amorphous Ru(bda)-polymer, limited access to the Ru(bda) moieties at the rough and disordered polymer interface (Figure S24) prevents the efficient dimerization of activated catalysts, thus restricting the water oxidation catalysis to a less efficient WNA mechanism. For Ru(bda)-COF however, the spherical morphology and smooth interfaces in extended crystalline domains still enable the interaction of two metal oxides following an interparticle I2M pathway. Catalysis initially starts with Ru(II) that is stepwise-oxidized to Ru(V) oxo species. After the release of oxygen from the dimeric intermediate, Ru(III) and Ru(IV) states are released, which can directly be subjected to the next catalytic cycle (Figure 5a). The composition and electronic state of Ru(bda)-COF before and after the catalysis were confirmed by X-ray photoelectron spectroscopy (XPS) measurements. The high-resolution XPS spectra of the O 1s, N 1s, Ru 2p, Ru 3d/C 1s, and Ru 4d/O 2p binding energy regions are shown in Figure 5c,d and Figure S54. The characteristic Ru 3d5/2 peak shifts from 278 to 279.5 eV before and after the catalysis, respectively, thus indicating a change in oxidation state from Ru(II) to Ru(III) (Figure 5c). This is consistent with the Ru 3d3/2 behavior (overlaid by additional C 1s contributions) as well as with a low energy shift of the O 2p valence band in Figure 5d.[36] Solid-state UV−vis diffuse reflectance (DR) spectroscopy also confirmed the change in the oxidation state of Ru(bda)-COF (Figure S55). Due to the change from Ru(II) to Ru(III), there is a facile ligand-to-metal charge transfer (LMCT) resulting in a red shift in absorption after catalysis. During both chemical and photochemical water oxidation, the long-range order and

https://doi.org/10.1021/jacs.2c07282
J. Am. Chem. Soc. 2022, 144, 17661−17670

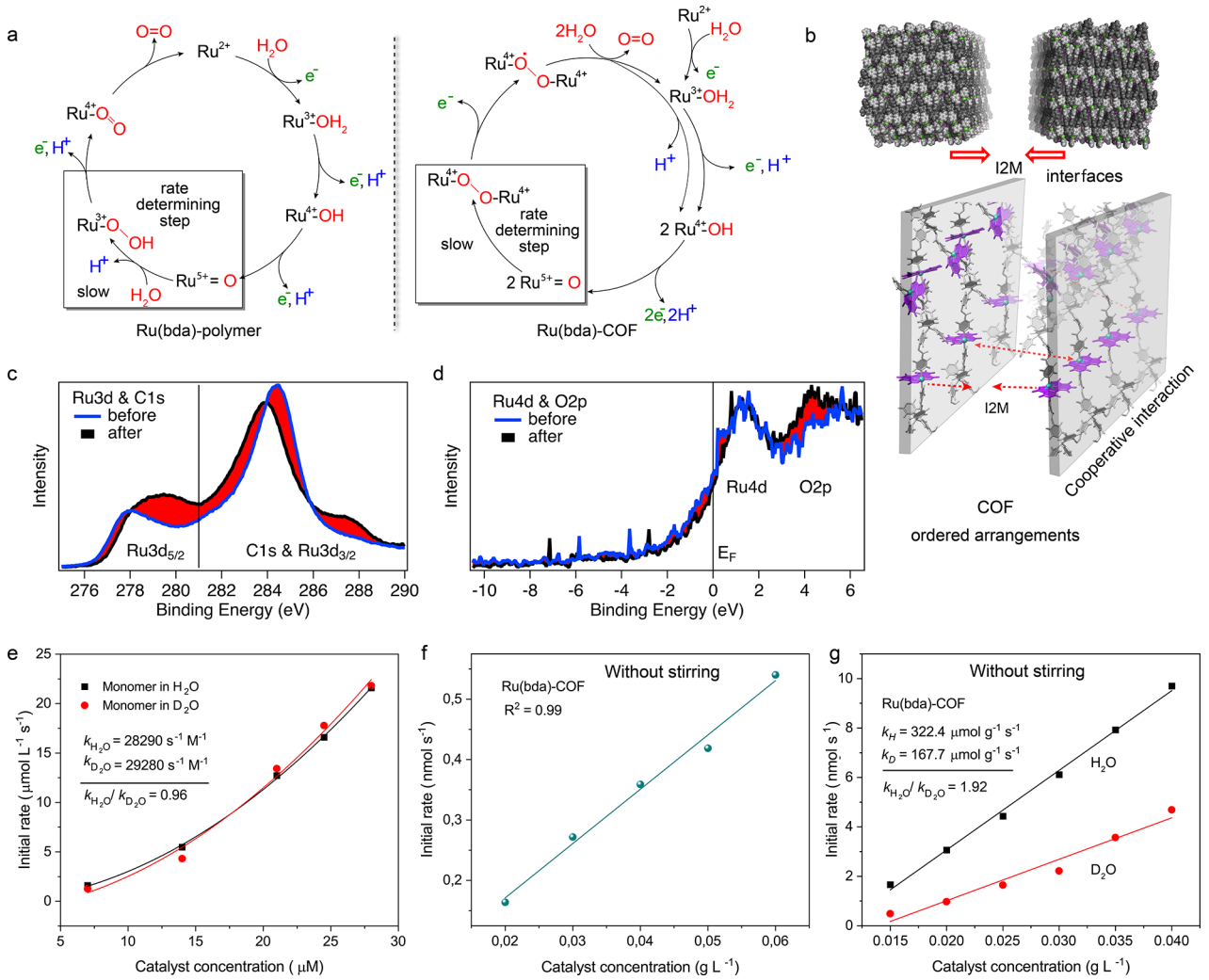

Figure 5. Proposed mechanism for water oxidation with Ru(bda)-based WOCs. (a) Mechanism of WNA and I2M pathways during catalytic water oxidation for Ru(bda)-polymer and Ru(bda)-COF, respectively. (b) Cartoon representation of the cooperative interaction of metal centers at the interface between different Ru(bda)-COF interfaces. (c, d) High-resolution XPS spectra of Ru(bda)-COF for regions Ru 3d/C 1s and Ru 4d/O 2p, respectively. (e) Plots of initial catalysis rates versus Ru(bda)-monomer concentration (the kinetic isotope effect was estimated from the linear regression fit for the plot of initial rates versus square of monomer concentration (Figure S48b)). (f) Plot of initial catalysis rates (obtained by linear fit of O_2 evolution curve between 145 and 155 s without any stirring during the measurement) versus Ru(bda)-COF concentration with corresponding linear regression fit. (g) Plots of initial catalysis rates versus Ru(bda)-COF concentration in H_2O and D_2O (first-order rate constants were determined by linear regression fit for plots of initial rates versus Ru(bda)-COF concentration).

periodic arrangement of molecular Ru(bda) WOCs throughout the COF domains make it possible that the crucial peroxo bond formation between two metal oxo units can occur in a concurrent fashion at multiple surface sites (Figure 5c and Figure S45). Unlike the previously reported heterogeneous systems,[13,15,37] for which the photocatalysis generally proceeds inside the pores and might be limited by diffusion, the uniform structure and morphology of Ru(bda)-COF trigger the catalysis at the smooth interfaces. In a highly cooperative fashion, the zipper-type alignment of the catalytic units simultaneously activates multiple sites for O−O bond formation, thus further enhancing the catalytic performance of the Ru(bda)-COF particles. The spherical morphology of Ru(bda)-COF facilitates the diffusion of the COF particles in solution, thus enhancing the likelihood for interparticle collisions (Figure 5b). Therefore, smaller particle sizes at a particular WOC concentration should lead to an enhancement of catalytic performance due to faster diffusion and a more favorable surface-to-volume ratio.

To test this hypothesis, we prepared two samples of Ru(bda)-COF with different particle size distribution by membrane filtration of sonicated COF suspensions. Indeed, photochemical water oxidation for COF particles in the range of 0.5−1 μm (Figures S40 and S41) and smaller than 0.5 μm (Figures S42 and S43) revealed an increased performance with decreasing particle size and second-order rate constants of 1169 and 1591 μmol L g^{-2} s^{-1} for the two samples. To investigate the influence of interparticle collisions on the catalytic activity, we have performed photocatalytic water oxidation for Ru(bda)-COF suspensions without any stirring. Interestingly, the initial rate drops down significantly from 3.21 to 0.54 μmol L^{-1} s^{-1} at 0.06 g L^{-1} Ru(bda)-COF concentration with and without stirring, respectively (Figure S44). Even more intriguingly, the initial rate shows now a linear dependency on Ru(bda)-COF concentration (Figure 5f and Figure S44b) and the KIE of 1.92 (Figure 5g and Figure S51) clearly indicates a switch to the WNA mechanism by merely switching the agitation. Apparently, stirring greatly

https://doi.org/10.1021/jacs.2c07282
J. Am. Chem. Soc. 2022, 144, 17661−17670

enhances the possibility for collisions between individual particles, thus facilitating the proposed I2M mechanism. Without agitation however, the COF nanoparticles sediment and water oxidation is limited to a less effective WNA pathway similar to the amorphous polymer. The obtained first-order rate constant (8.9 μmol g^{-1} s^{-1}) is higher than that of Ru(bda)-polymer (3.0 μmol g^{-1} s^{-1}). This could be due to the smoother surface for the COF, which provides more accessible sites for the WNA mechanism.

As a molecular control, we have further synthesized a Ru(bda)-diimine complex following the standard reaction of imine condensation with 4-*tert*-butylaniline (Scheme S4). This monomer has the similar bond connectivity as Ru(bda)-COF. It has been observed that the initial rate for this control increases also quadratically during photocatalytic water oxidation (Figure S53a–c). The KIE measurements show that the k_{H_2O}/k_{D_2O} ratio is 0.96 (Figure 5e and Figures S47 and S48). Thus, no protons are involved in the dimerization of two metal oxides in the RDS. This is similar to the oxygen formation pathway during COF-catalyzed water oxidation. To further probe the particular activity of the Ru(bda) units and any cooperative effects, we measured chemical water oxidation of dialdehyde precursor **1** as another molecular model compound. As expected, **1** proves to be an efficient WOC following the I2M mechanism (Figure S52a) with a second-order rate constant of $k_1 = 1.48 \times 10^5$ L mol^{-1} s^{-1}. We have further performed H/D KIE measurements using the Ru(bda) dialdehyde precursor **1**, showing a KIE of 0.98 for the free ligand (Figures S49 and S50). This experimental evidence firmly supports the I2M pathway of water oxidation for COF. For crystalline Ru(bda)-COF, a lower rate constant of $k_{Ru(bda)\text{-}COF} = 8.50 \times 10^2$ L mol^{-1} s^{-1} was obtained when considering all Ru centers. For the proposed I2M mechanism however, water oxidation is restricted to the accessible sites at the nanoparticle interfaces. Thus, we have estimated the ratio between the surface and bulk Ru for spherical nanoparticles of different sizes. Based on a simple structural model derived from PXRD data, we calculated bulk and surface densities of 1.12 Ru per nm^{-3} and 1.06 Ru per nm^{-2} for the crystalline Ru(bda)-COF phases (cuboid unit cell with $a = b = 1.9$ nm and $c = 19.79$ nm, eight Ru in the unit cell and four Ru available for each face of the unit cell, see Structure Simulation for details). From these values and the formulas for the volume ($4/3 \cdot \pi \cdot r^3$) and surface ($4 \cdot \pi \cdot r^2$) of a sphere, we obtained surface-to-volume ratios of 0.03 and 0.015 for nanoparticles with 200 and 400 nm diameters, respectively. To estimate the activity of the catalytically active surface sites, we adjusted the concentration of Ru for the maximum amount available at the nanoparticle interfaces and plotted the initial rate of O_2 evolution against the square of this effective concentration to obtain second-order rate constants $k_{surface}$ in the range of $0.94–3.78 \times 10^6$ L mol^{-1} s^{-1} (Figure S52). The approximately 10-fold increase in molecular activity after implementing **1** within Ru(bda)-COF clearly indicates the proposed cooperative effect of the ordered alignment of well-defined Ru catalysts in crystalline frameworks. In reality, this effect should be even higher as the actual amount of accessible Ru catalysts at the interface will be lower due to grain boundaries (crystallite size of ~15 nm, see Figures S32 and S33) and other defects.

The immobilization of molecular Ru(bda) units in extended 3D imine frameworks turned out to be an excellent strategy for preparation of highly active and durable heterogeneous WOCs. For amorphous Ru(bda)-polymer, the photochemical activity of 0.5 μmol L^{-1} s^{-1} at a low catalyst loading of 0.1 g L^{-1} is already 500 times higher as the best COF-based WOC to date and comparable to the benchmark H_2-evolving frameworks (Tables S9 and S10). Even more impressively, the crystalline Ru(bda)-COF outperforms both the benchmark H_2- and O_2-evolving COF systems by 25- and 10,500-fold increases of initial rates.

CONCLUSIONS

In summary, we have for the first time integrated highly active Ru(bda) catalysts as integral subcomponents into 3D imine polymers. Depending on the reaction solvent, amorphous Ru(bda)-polymer or crystalline Ru(bda)-COF were isolated after isothermal imine condensation. The amorphous structure showed only modest activity in both chemical and photochemical water oxidation as the disordered distribution of the Ru centers limits water oxidation to the slow WNA pathway. For the precisely designed crystalline COF however, the periodicity of the atomically pinpoint framework allows for a cooperative interplay of multiple active sites for a facile water oxidation via the I2M mechanism. The 5-fold interpenetration of the dia-network significantly enhances the stability as the heterogeneous catalyst could be recycled for several cycles without any loss of activity. This modular design approach might also be applied to the efficient immobilization of other highly active molecular catalysts to combine molecular precision with heterogeneous durability and processability.

ASSOCIATED CONTENT

Supporting Information

The Supporting Information is available free of charge at https://pubs.acs.org/doi/10.1021/jacs.2c07282.

Synthetic methods, characterizations, electrochemical techniques, and chemical and photochemical water oxidation methods (PDF)

AUTHOR INFORMATION

Corresponding Authors

Florian Beuerle − *Institut für Organische Chemie, Julius-Maximilians-Universität Würzburg, Würzburg 97074, Germany; Center for Nanosystems Chemistry (CNC), Julius-Maximilians-Universität Würzburg, Würzburg 97074, Germany;* orcid.org/0000-0001-7239-8327; Email: florian.beuerle@uni-wuerzburg.de

Frank Würthner − *Institut für Organische Chemie, Julius-Maximilians-Universität Würzburg, Würzburg 97074, Germany; Center for Nanosystems Chemistry (CNC), Julius-Maximilians-Universität Würzburg, Würzburg 97074, Germany;* orcid.org/0000-0001-7245-0471; Email: wuerthner@uni-wuerzburg.de

Authors

Suvendu Karak − *Institut für Organische Chemie, Julius-Maximilians-Universität Würzburg, Würzburg 97074, Germany*

Vladimir Stepanenko − *Institut für Organische Chemie, Julius-Maximilians-Universität Würzburg, Würzburg 97074, Germany*

Matthew A. Addicoat − *School of Science and Technology, Nottingham Trent University, Nottingham NG11 8NS, U.K.;* orcid.org/0000-0002-5406-7927

Philipp Keßler − *Physikalisches Institut and Würzburg-Dresden Cluster of Excellence ct.qmat, Universität Würzburg, Würzburg D-97074, Germany*

Simon Moser − *Physikalisches Institut and Würzburg-Dresden Cluster of Excellence ct.qmat, Universität Würzburg, Würzburg D-97074, Germany*

Complete contact information is available at: https://pubs.acs.org/10.1021/jacs.2c07282

Author Contributions

All authors have given approval to the final version of the manuscript.

Funding

This research was funded by the European Research Council (ERC) under the European Union's Horizon 2020 Research and Innovation Program (SUPRAWOC, grant agreement no. 787937). We also acknowledge the supports from the Bavarian State Ministry of Science, Research, and the Arts for the Collaborative Research Network "Solar Technologies go Hybrid". S.K. thanks the Alexander von Humboldt Foundation for a postdoctoral fellowship, M.A.A. thanks the UK Materials and Molecular Modelling Hub for computational resources via EPSRC (EP/T022213), and S.M. acknowledges DFG, German Research Foundation (EXC 2147, Project ID 390858490).

Notes

The authors declare no competing financial interest.

REFERENCES

(1) Kärkäs, M. D.; Verho, O.; Johnston, E. V.; Åkermark, B. Artificial Photosynthesis: Molecular Systems for Catalytic Water Oxidation. *Chem. Rev.* **2014**, *114*, 11863−12001.

(2) Barber, J. Photosynthetic energy conversion: natural and artificial. *Chem. Soc. Rev.* **2009**, *38*, 185−196.

(3) Llobet, A. *Molecular Water Oxidation Catalysis*; John Wiley & Sons Ltd.: New York, 2014.

(4) Blakemore, J. D.; Crabtree, R. H.; Brudvig, G. W. Molecular Catalysts for Water Oxidation. *Chem. Rev.* **2015**, *115*, 12974−13005.

(5) Yin, Q.; Tan Jeffrey, M.; Besson, C.; Geletii Yurii, V.; Musaev Djamaladdin, G.; Kuznetsov Aleksey, E.; Luo, Z.; Hardcastle Ken, I.; Hill Craig, L. A Fast Soluble Carbon-Free Molecular Water Oxidation Catalyst Based on Abundant Metals. *Science* **2010**, *328*, 342−345.

(6) Matheu, R.; Ertem, M. Z.; Gimbert-Suriñach, C.; Sala, X.; Llobet, A. Seven Coordinated Molecular Ruthenium−Water Oxidation Catalysts: A Coordination Chemistry Journey. *Chem. Rev.* **2019**, *119*, 3453−3471.

(7) Zhang, B.; Sun, L. Ru-bda: Unique Molecular Water-Oxidation Catalysts with Distortion Induced Open Site and Negatively Charged Ligands. *J. Am. Chem. Soc.* **2019**, *141*, 5565−5580.

(8) Sheridan, M. V.; Sherman, B. D.; Fang, Z.; Wee, K.-R.; Coggins, M. K.; Meyer, T. J. Electron Transfer Mediator Effects in the Oxidative Activation of a Ruthenium Dicarboxylate Water Oxidation Catalyst. *ACS Catal.* **2015**, *5*, 4404−4409.

(9) Schindler, D.; Gil-Sepulcre, M.; Lindner, J. O.; Stepanenko, V.; Moonshiram, D.; Llobet, A.; Würthner, F. Efficient Electrochemical Water Oxidation by a Trinuclear Ru(bda) Macrocycle Immobilized on Multi-Walled Carbon Nanotube Electrodes. *Adv. Energy Mater.* **2020**, *10*, 2002329.

(10) Sévery, L.; Szczerbiński, J.; Taskin, M.; Tuncay, I.; Brandalise Nunes, F.; Cignarella, C.; Tocci, G.; Blacque, O.; Osterwalder, J.; Zenobi, R.; Iannuzzi, M.; Tilley, S. D. Immobilization of molecular catalysts on electrode surfaces using host−guest interactions. *Nat. Chem.* **2021**, *13*, 523−529.

(11) Bonchio, M.; Syrgiannis, Z.; Burian, M.; Marino, N.; Pizzolato, E.; Dirian, K.; Rigodanza, F.; Volpato, A. G.; Ganga, G. L.; Demitri, N.; Berardi, S.; Amenitsch, H.; Guldi, D. M.; Caramori, S.; Bignozzi, A. C.; Sartorel, A.; Prato, M. Hierarchical organization of perylene bisimides and polyoxometalates for photo-assisted water oxidation. *Nat. Chem.* **2019**, *11*, 146−153.

(12) Ashford, D. L.; Sherman, B. D.; Binstead, R. A.; Templeton, J. L.; Meyer, T. J. Electro-assembly of a chromophore-catalyst bilayer for water oxidation and photocatalytic water splitting. *Angew. Chem., Int. Ed.* **2015**, *54*, 4778−4781.

(13) Li, F.; Fan, K.; Wang, L.; Daniel, Q.; Duan, L.; Sun, L. Immobilizing Ru(bda) Catalyst on a Photoanode via Electrochemical Polymerization for Light-Driven Water Splitting. *ACS Catal.* **2015**, *5*, 3786−3790.

(14) Schulze, M.; Kunz, V.; Frischmann, P. D.; Würthner, F. A supramolecular ruthenium macrocycle with high catalytic activity for water oxidation that mechanistically mimics photosystem II. *Nat. Chem.* **2016**, *8*, 576−583.

(15) Lin, L.; Lin, Z.; Zhang, J.; Cai, X.; Lin, W.; Yu, Z.; Wang, X. Molecular-level insights on the reactive facet of carbon nitride single crystals photocatalysing overall water splitting. *Nat. Catal.* **2020**, *3*, 649−655.

(16) Wang, X.; Maeda, K.; Thomas, A.; Takanabe, K.; Xin, G.; Carlsson, J. M.; Domen, K.; Antonietti, M. A metal-free polymeric photocatalyst for hydrogen production from water under visible light. *Nat. Mater.* **2009**, *8*, 76−80.

(17) Vyas, V. S.; Haase, F.; Stegbauer, L.; Savasci, G.; Podjaski, F.; Ochsenfeld, C.; Lotsch, B. V. A tunable azine covalent organic framework platform for visible light-induced hydrogen generation. *Nat. Commun.* **2015**, *6*, 8508.

(18) Yang, J.; Acharjya, A.; Ye, M.-Y.; Rabeah, J.; Li, S.; Kochovski, Z.; Youk, S.; Roeser, J.; Grüneberg, J.; Penschke, C.; Schwarze, M.; Wang, T.; Lu, Y.; van de Krol, R.; Oschatz, M.; Schomäcker, R.; Saalfrank, P.; Thomas, A. Protonated Imine-Linked Covalent Organic Frameworks for Photocatalytic Hydrogen Evolution. *Angew. Chem., Int. Ed.* **2021**, *60*, 19797−19803.

(19) Wang, X.; Chen, L.; Chong, S. Y.; Little, M. A.; Wu, Y.; Zhu, W.-H.; Clowes, R.; Yan, Y.; Zwijnenburg, M. A.; Sprick, R. S.; Cooper, A. I. Sulfone-containing covalent organic frameworks for photocatalytic hydrogen evolution from water. *Nat. Chem.* **2018**, *10*, 1180−1189.

(20) Jin, E.; Lan, Z.; Jiang, Q.; Geng, K.; Li, G.; Wang, X.; Jiang, D. 2D sp^2 Carbon-Conjugated Covalent Organic Frameworks for Photocatalytic Hydrogen Production from Water. *Chem* **2019**, *5*, 1632−1647.

(21) Li, S.; Chen, B.; Wang, Y.; Ye, M.-Y.; van Aken, P. A.; Cheng, C.; Thomas, A. Oxygen-evolving catalytic atoms on metal carbides. *Nat. Mater.* **2021**, *20*, 1240−1247.

(22) Xie, J.; Shevlin, S. A.; Ruan, Q.; Moniz, S. J. A.; Liu, Y.; Liu, X.; Li, Y.; Lau, C. C.; Guo, Z. X.; Tang, J. Efficient visible light-driven water oxidation and proton reduction by an ordered covalent triazine-based framework. *Energy Environ. Sci.* **2018**, *11*, 1617−1624.

(23) Wan, Y.; Wang, L.; Xu, H.; Wu, X.; Yang, J. A Simple Molecular Design Strategy for Two-Dimensional Covalent Organic Framework Capable of Visible-Light-Driven Water Splitting. *J. Am. Chem. Soc.* **2020**, *142*, 4508−4516.

(24) Sick, T.; Hufnagel, A. G.; Kampmann, J.; Kondofersky, I.; Calik, M.; Rotter, J. M.; Evans, A.; Döblinger, M.; Herbert, S.; Peters, K.; Böhm, D.; Knochel, P.; Medina, D. D.; Fattakhova-Rohlfing, D.; Bein, T. Oriented Films of Conjugated 2D Covalent Organic Frameworks as Photocathodes for Water Splitting. *J. Am. Chem. Soc.* **2018**, *140*, 2085−2092.

(25) Krishnaraj, C.; Sekhar Jena, H.; Bourda, L.; Laemont, A.; Pachfule, P.; Roeser, J.; Chandran, C. V.; Borgmans, S.; Rogge, S. M. J.; Leus, K.; Stevens, C. V.; Martens, J. A.; Van Speybroeck, V.; Breynaert, E.; Thomas, A.; Van Der Voort, P. Strongly Reducing (Diarylamino)benzene-Based Covalent Organic Framework for Metal-Free Visible Light Photocatalytic H_2O_2 Generation. *J. Am. Chem. Soc.* **2020**, *142*, 20107−20116.

(26) Lan, Z. A.; Fang, Y.; Zhang, Y.; Wang, X. Photocatalytic Oxygen Evolution from Functional Triazine-Based Polymers with Tunable Band Structures. *Angew. Chem., Int. Ed.* **2018**, *57*, 470−474.

(27) Bi, S.; Yang, C.; Zhang, W.; Xu, J.; Liu, L.; Wu, D.; Wang, X.; Han, Y.; Liang, Q.; Zhang, F. Two-dimensional semiconducting covalent organic frameworks via condensation at arylmethyl carbon atoms. *Nat. Commun.* **2019**, *10*, 2467.
(28) Banerjee, T.; Podjaski, F.; Kröger, J.; Biswal, B. P.; Lotsch, B. V. Polymer photocatalysts for solar-to-chemical energy conversion. *Nat. Rev. Mater.* **2021**, *6*, 168−190.
(29) Côté, A. P.; Benin, A.; Ockwig, N.; O'Keeffe, M.; Matzger, A.; Yaghi, O. Porous, Crystalline, Covalent Organic Frameworks. *Science* **2005**, *310*, 1166−1170.
(30) Jin, E.; Asada, M.; Xu, Q.; Dalapati, S.; Addicoat, M. A.; Brady, M.; Xu, H.; Nakamura, T.; Heine, T.; Chen, Q.; Jiang, D. Two-dimensional sp^2 carbon−conjugated covalent organic frameworks. *Science* **2017**, *357*, 673−676.
(31) Xu, H.; Gao, J.; Jiang, D. Stable, crystalline, porous, covalent organic frameworks as a platform for chiral organocatalysts. *Nat. Chem.* **2015**, *7*, 905−912.
(32) Sasmal, H. S.; Bag, S.; Chandra, B.; Majumder, P.; Kuiry, H.; Karak, S.; Sen Gupta, S.; Banerjee, R. Heterogeneous C−H Functionalization in Water via Porous Covalent Organic Framework Nanofilms: A Case of Catalytic Sphere Transmutation. *J. Am. Chem. Soc.* **2021**, *143*, 8426−8436.
(33) Halder, A.; Karak, S.; Addicoat, M.; Bera, S.; Chakraborty, A.; Kunjattu, S. H.; Pachfule, P.; Heine, T.; Banerjee, R. Ultrastable Imine-Based Covalent Organic Frameworks for Sulfuric Acid Recovery: An Effect of Interlayer Hydrogen Bonding. *Angew. Chem., Int. Ed.* **2018**, *57*, 5797−5802.
(34) Ma, T.; Kapustin, E. A.; Yin, S. X.; Liang, L.; Zhou, Z.; Niu, J.; Li, L.-H.; Wang, Y.; Su, J.; Li, J.; Wang, X.; Wang, W. D.; Wang, W.; Sun, J.; Yaghi, O. M. Single-crystal x-ray diffraction structures of covalent organic frameworks. *Science* **2018**, *361*, 48−52.
(35) Garai, B.; Shetty, D.; Skorjanc, T.; Gándara, F.; Naleem, N.; Varghese, S.; Sharma, S. K.; Baias, M.; Jagannathan, R.; Olson, M. A.; Kirmizialtin, S.; Trabolsi, A. Taming the Topology of Calix[4]arene-Based 2D-Covalent Organic Frameworks: Interpenetrated vs Non-interpenetrated Frameworks and Their Selective Removal of Cationic Dyes. *J. Am. Chem. Soc.* **2021**, *143*, 3407−3415.
(36) Jovic, V.; Consiglio, A.; Smith, K. E.; Jozwiak, C.; Bostwick, A.; Rotenberg, E.; Di Sante, D.; Moser, S. Momentum for Catalysis: How Surface Reactions Shape the RuO_2 Flat Surface State. *ACS Catal.* **2021**, *11*, 1749−1757.
(37) Banerjee, T.; Gottschling, K.; Savasci, G.; Ochsenfeld, C.; Lotsch, B. V. H_2 Evolution with Covalent Organic Framework Photocatalysts. *ACS Energy Lett.* **2018**, *3*, 400−409.

https://doi.org/10.1021/jacs.2c07282
J. Am. Chem. Soc. 2022, 144, 17661−17670